Mineralogical Magazine (2023), **87**, 130–142
doi:10.1180/mgm.2022.125

CAMBRIDGE UNIVERSITY PRESS

Article

Dark-coloured Mn-rich overgrowths in an elbaitic tourmaline crystal from the Rosina pegmatite, San Piero in Campo, Elba Island, Italy: witness of late-stage opening of the geochemical system

Alessandra Altieri[1]*, Federico Pezzotta[2], Henrik Skogby[3], Ulf Hålenius[3] and Ferdinando Bosi[1]

[1]Department of Earth Sciences, Sapienza University of Rome, Piazzale Aldo Moro 5, I-00185 Rome, Italy; [2]Natural History Museum, Corso Venezia 55, 20121 Milan, Italy; and [3]Department of Geosciences, Swedish Museum of Natural History, Box 50007, SE-10405 Stockholm, Sweden

Abstract

Multicoloured tourmalines from Elba Island, commonly display dark-coloured terminations due to incorporation of Fe, and also occasionally Mn. The mechanisms which led to the availability of these elements in the late-stage residual fluids are not yet completely understood. For this purpose, we investigated a representative tourmaline crystal found naturally in two fragments within a wide miarolitic cavity in the Rosina pegmatite (San Piero in Campo, Elba Island, Italy), and characterised by late-stage dark-coloured overgrowths. Microstructural and paragenetic observations, together with compositional and spectroscopic data (electron microprobe and optical absorption spectroscopy), provide evidence which shows that the formation of the dark-coloured Mn-rich overgrowths are the result of a pocket rupture. This event caused alteration of the cavity-coating spessartine garnet by highly-reactive late-stage cavity fluids by leaching processes, with the subsequent release of Mn to the residual fluids. We argue that the two fragments were originally a single crystal, which underwent natural breakage followed by the simultaneous growth of Mn-rich dark terminations at both breakage surfaces. This conclusion supports the evidence for a pocket rupture event, responsible for both the shattering of the tourmaline crystal and the compositional variation of the cavity-fluids related to the availability of Mn, which was incorporated by the tourmaline crystals. Additionally, a comparison of the dark overgrowths formed at the analogous and the antilogous poles, provides information on tourmaline crystallisation at the two different poles. The antilogous pole is characterised by a higher affinity for Ca, F and Ti, and a selective uptake of Mn^{2+}, even in the presence of a considerable amount of Mn^{3+} in the system. This uneven uptake of Mn ions resulted in the yellow–orange colouration of the antilogous overgrowth (Mn^{2+} dependent) rather than the purple-reddish colour of the analogous overgrowths (Mn^{3+} dependent).

Keywords: tourmaline, electron microprobe, optical absorption spectroscopy, granitic pegmatites, miarolitic cavities, Elba Island

(Received 18 August 2022; accepted 6 November 2022; Accepted Manuscript published online: 28 November 2022; Associate Editor: František Laufek)

Introduction

Tourmaline is the most widespread borosilicate mineral in the Earth's crust, typically occurring in granites and granite pegmatites as well as in sedimentary and metamorphic rocks (van Hinsberg *et al.*, 2011a, 2011b; Dutrow and Henry, 2018; Henry and Dutrow, 2018). The compositional complexity of this mineral arises from its general formula, which can be written as $XY_3Z_6T_6O_{18}(BO_3)_3V_3W$, where $X = Na^+$, K^+, Ca^{2+}, $\square$ (= vacancy); $Y = Mg^{2+}$, Fe^{2+}, Mn^{2+}, Li^+, Al^{3+}, Fe^{3+}, Cr^{3+}, V^{3+}, Ti^{4+}; $Z = Al^{3+}$, Fe^{3+}, Cr^{3+}, V^{3+}, Mg^{2+}, Fe^{2+}; $T = Si^{4+}$, Al^{3+}, B^{3+}; $B = B^{3+}$; $V = (OH)^-$, O^{2-}; and $W = (OH)^-$, F^-, O^{2-}.

Due to the occurrence of an extensive short-range order, which can impose extremely slow diffusion rates of the constituents in the structure, tourmalines can, once formed, retain their original composition (e.g. Hawthorne and Dirlam, 2011; van Hinsberg *et al.*, 2011a, 2011b; Bosi, 2018). Thus, they are able to preserve the chemical-physical variation of the crystallisation environment during crystal growth (e.g. Agrosì *et al.*, 2006). Moreover, the extensive $P–T$ stability range of tourmalines make them an efficient geological tool for investigating $P–T–X$ conditions in all crustal settings within the Earth (van Hinsberg *et al.*, 2011a, 2011b). As a result, tourmaline is an excellent petrogenetic indicator that can provide information about the formation and evolution of complex crystals over time, acting as a 'geologic DVD' (Dutrow and Henry, 2011).

Multicoloured tourmalines of pastel or light colours with dark crystal terminations at the analogous pole (the $\mathbf{c}^-$ side of the crystal) are characteristics of Elba Island pegmatites, Italy. These terminations are usually black, though can appear in different colours such as brown, green, red–violet, and blue. Such more-or-less dark-coloured terminations may occur as narrow overgrowths, but can also compose a significant zone of the

*Author for correspondence: Alessandra Altieri, Email: alessandra.altieri@uniroma1.it
Cite this article: Altieri A., Pezzotta F., Skogby H., Hålenius U. and Bosi F. (2023) Dark-coloured Mn-rich overgrowths in an elbaitic tourmaline crystal from the Rosina pegmatite, San Piero in Campo, Elba Island, Italy: witness of late-stage opening of the geochemical system. *Mineralogical Magazine* **87**, 130–142. https://doi.org/10.1180/mgm.2022.125

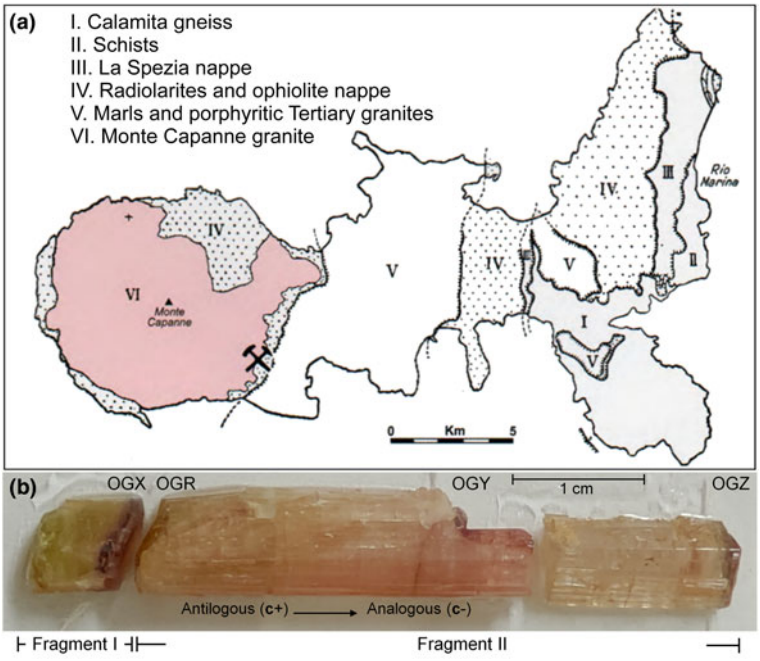

Fig. 1. (a) Geological map of Elba Island. The occurrence area of the analysed tourmaline samples (San Piero in Campo, Elba Island, Italy) is marked at the edge of the Monte Capanne granite (after Trevisan, 1951 and modified by Pezzotta, 2021). (b) The analysed tourmaline crystal fragments. The first fragment (7 mm in length) was collected as it is (fragment I), whereas the other two parts (30 and 15 mm in length, respectively) were originally connected as a single fragment (fragment II) that broke during collection from the pocket. OGX, OGY, OGZ and OGR indicate the dark-coloured overgrowths. Scale bar = 1 cm.

crystals, such as in the case of some elbaite crystals which are overgrown by aggregates of long parallel needles (Pezzotta, 2021).

The formation of the dark-coloured overgrowths in Elba tourmalines is related to physico-chemical variations in the crystallisation environment during the latest stages of tourmaline crystal growth. Such changes are consequent to the partial destabilisation of the pocket environment in which the tourmalines grew. The opening of the geochemical system due to pocket rupture has been suggested by several authors. However, the detailed events that led to chemical changes in the pocket environment resulting in the growth of late-stage tourmalines remain unclear. Some authors propose that fracturing of the pocket allowed the introduction of external fluids coming from other regions of consolidated pegmatite that infiltrated the host rock and modified the chemical environment (e.g. Foord 1976; Aurisicchio *et al.*, 1999; Selway *et al.*, 1999; London, 2006). In accord with this view, Dutrow and Henry (2000, 2016, 2018) proposed that external fluids reacted with the host-rock and, in these conditions, tourmaline crystals dissolved to alter their composition with the generation of a late-stage fibrous Fe-rich tourmaline characterised by an external fluid signature. In contrast, Novák and Taylor (2000) suggested that an internal source of Fe must be sought for the origin of Fe-rich late-stage tourmalines. In agreement with this latter consideration, Černý (2000) assessed that extensive leaching and corrosion of the cavity-lining and cavity-coating minerals of the pegmatite, could lead to variations in the composition of the cavity fluid. Buřival and Novák (2015) suggested that the chemical change in the cavity system is the result of hydrothermal alteration of the cavity-lining minerals by late-stage fluids, which developed in the final stages of pegmatite crystallisation. Additionally, Felch *et al.* (2016) inferred that the observed corrosion and leaching of cavity-lining spessartine garnet crystals, was the result of reactions with late-stage hydrothermal fluids that originated and migrated from adjacent highly evolved miarolitic cavities. More recently, Bosi *et al.* (2022) and Altieri *et al.* (2022) proposed that the pocket rupture event, possibly related to thermal contraction during the cooling of the rock, led to mechanical brittle deformation of the enclosing pegmatite by the formation of late-stage fractures. This allowed the highly-reactive late-stage cavity fluids to permeate the fractures surrounding the cavity where the early-crystallised cavity-lining and cavity-coating Fe- and Mn-rich minerals were hosted. Leaching and corrosion processes ascribed to the late-stage cavity fluids led to the hydrothermal alteration of such minerals, with the subsequent release of Fe, and occasionally Mn, in the pocket environment.

The relatively recent discovery of some cavities in the Rosina Pegmatite in San Piero in Campo allowed careful collection of many, mostly elbaitic, tourmaline crystals characterised by a variety of dark-coloured overgrowths. Paragenetic and structural information of the pegmatite were also recorded (Pezzotta, 2021). This investigation is focused on the crystal-chemical characterisation of an elbaitic multicoloured tourmaline crystal found in the cavity which has been naturally broken into two fragments. It is characterised by dark-coloured overgrowths, respectively purplish-red at the analogous pole, and yellow–orange at the antilogous pole. This crystal has also been selected because it is representative of the texture of the tourmaline crystals occurring in cavities of many other Elba pegmatites that underwent a similar chemico-physical evolution (Pezzotta, 2021).

In this investigation we correlated structural evidence, fracturing of the pocket producing breakage of tourmaline crystals, to the late-stage tourmaline generation.

Occurrence and sample description

The Rosina pegmatite is located a few hundred metres south of the San Piero in Campo village, Elba Island, Italy, and since its discovery in early 1990, has been mined for both collectibles and specimens suitable for scientific research (Pezzotta, 2021). The pegmatite is hosted in a porphyritic monzogranite at the eastern border of the Monte Capanne pluton (Fig. 1a) and has a complex shape, trending roughly N–S with a variable dip angle of 40–75°W (Pezzotta, 2000). The major productive section of the body is ~14 m long and 0.6–2.1 m wide. In general, the shallowest portions of the pegmatite body were characterised by mostly aplitic textures with minor coarse-grained pegmatitic

https://doi.org/10.1180/mgm.2022.125 Published online by Cambridge University Press

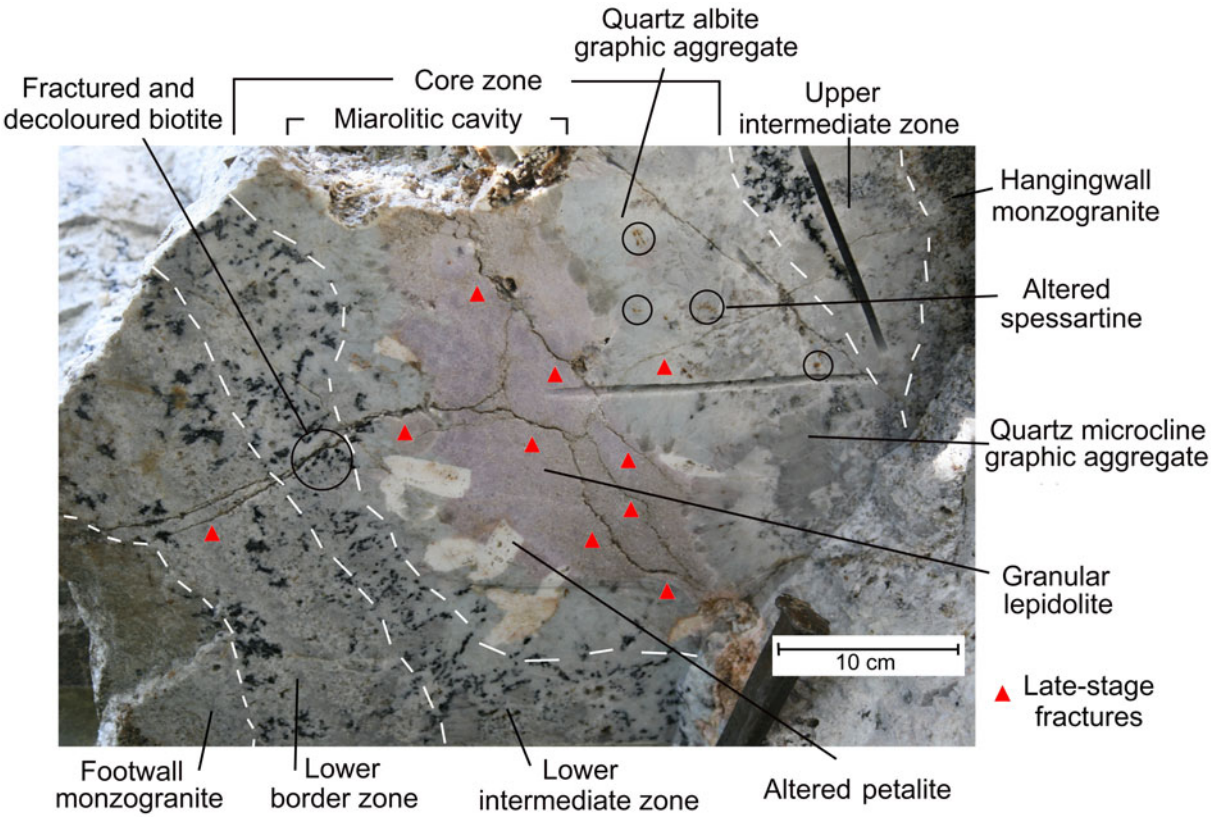

Fig. 2. E–W section of the Rosina pegmatite (~60 cm in thickness), with the different textures and mineralogical zonation labelled. The altered cavity-lining minerals as well as late-stage fractures (red arrows) are also marked. Scale bar = 10 cm.

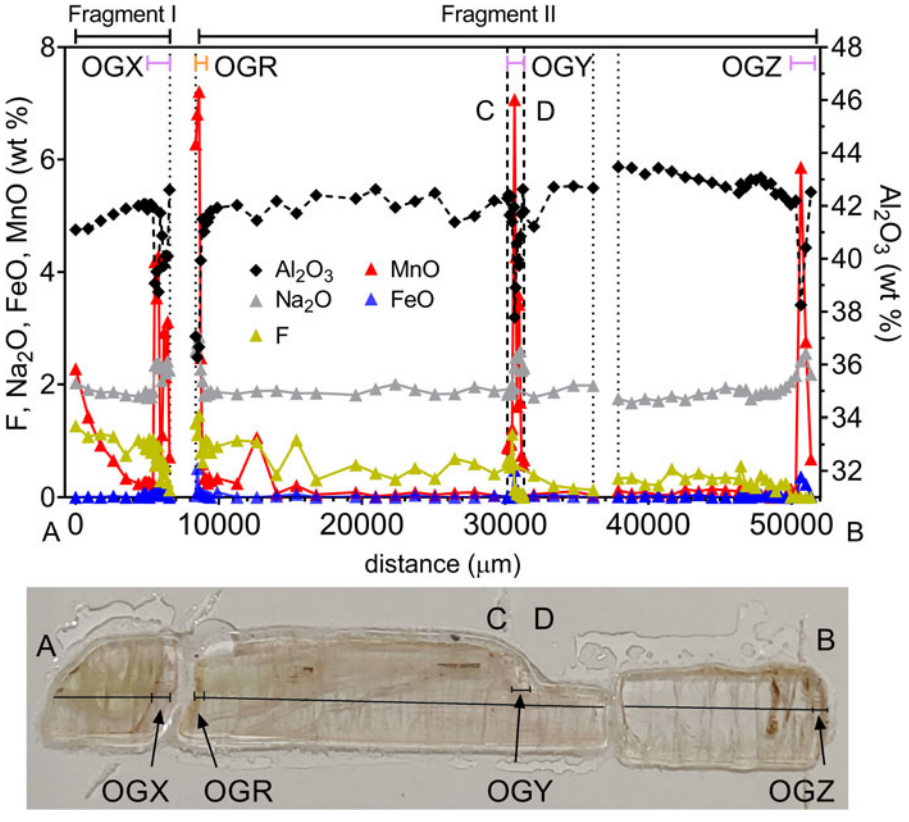

Fig. 3. Upper panel: results of compositional analysis of the tourmaline crystal fragments along two traverses (A–B and C–D). Lower panel: thin section of the analysed tourmaline fragments, with the traverses parallel to the **c**-axis represented by solid lines. OGX, OGR, OGY and OGZ are used for the different overgrowths.

https://doi.org/10.1180/mgm.2022.125 Published online by Cambridge University Press

Table 1. Representative compositions and atoms per formula unit (apfu) for the overgrowths OGX and OGR in the tourmaline crystals studied from San Piero in Campo, Elba Island, Italy. Average values and data for representative analysed spots are reported.

	OGX			OGR	
	spot #13	spot #20	Average $n = 9$	spot #23	Average $n = 5$
Length (μm)			~1000		~500
SiO_2 (wt.%)	37.29	38.04	37.88(30)	37.39	37.05(31)
TiO_2	0.20	0.02	0.10(7)	0.39	0.25(10)
B_2O_3 [a]	10.82	10.99	10.94	10.70	10.69
Al_2O_3	39.07	40.10	39.55(55)	36.27	37.48(39)
FeO_{tot}	0.10	0.10	0.10(5)	0.51	0.19(25)
MnO_{tot}	4.18	3.11	3.36(82)	6.81	5.69(47)
CaO	0.02	0.06	0.07(3)	0.34	0.20(10)
Na_2O	2.34	2.41	2.34(8)	2.74	2.61(13)
Li_2O [c]	1.56	1.70	1.71	1.41	1.46
K_2O	0.01	0.01	0.01(1)	0.02	0.02(1)
F	0.57	0.27	0.57(23)	1.12	1.17(17)
H_2O [a]	3.30	3.49	3.21	2.85	2.89
$-O \equiv F$	−0.24	−0.11	−0.24	−0.47	−0.49
MnO [d]	2.68	2.00	2.16	6.18	5.69
Mn_2O_3 [d]	1.67	1.24	1.34	–	–
Total	99.27	100.20	99.62	100.16	99.25
Atoms normalised to 31 anions					
Si (apfu)	5.990	6.015	6.021	6.073	6.023
Ti^{4+}	0.024	0.003	0.012	0.048	0.030
B	3.000	3.000	3.000	3.000	3.000
Al	7.396	7.472	7.418	6.943	7.182
Fe^{3+} [b]	0.013	0.013	0.013	–	–
Fe^{2+} [b]	–	–	–	0.077	0.026
Mn^{3+}	0.204	0.149	0.162	–	–
Mn^{2+}	0.365	0.268	0.290	0.937	0.784
Ca	0.004	0.010	0.011	0.059	0.035
Na	0.728	0.740	0.720	0.863	0.824
Li	1.008	1.081	1.093	0.921	0.955
K	0.002	0.003	0.003	0.004	0.003
F	0.289	0.134	0.287	0.573	0.603
OH	3.537	3.676	3.404	3.171	3.131

[a]Calculated by stoichiometry (see text)
[b]All Fe was considered to be Fe^{3+}, with the exception of the OGR overgrowth, based on the OAS results
[c]Estimated with the procedure of Pesquera *et al.* (2016)
[d]Determined by OAS
Errors for oxides and fluorine are standard deviations (in brackets); '–' indicates not detected.

lenses, whereas at greater depths, the body becomes more pegmatitic and divides into two major branches that are interconnected by several small veinlets (Pezzotta, 2000; Bosi *et al.*, 2022).

The Rosina pegmatite belongs to the LCT family. This pegmatite is commonly miarolitic, with abundant small to medium size pockets and a series of medium to large pockets (up to ~80 dm^3 in volume), and is significantly asymmetric in terms of textures, mineralogy and geochemistry. The axial core–miarolitic zone, which is rich in lepidolite, petalite and pollucite, divides the body into a medium-grained lower section enriched in albite with minor K-feldspar, quartz, spessartine, patches of sekaninaite and comb-texture tourmaline, and an upper coarse-grained section enriched in feldspar with minor albite, quartz and tourmaline. Cavities found at shallower levels contain dark-coloured tourmalines, together with pale-blue aquamarine and spessartine. In contrast, cavities found at deeper levels contain abundant polychrome and rose tourmalines with variable Mn and Fe content, morganite, petalite, pollucite and spessartine (Orlandi and Pezzotta, 1996; Pezzotta, 2000; Bosi *et al.*, 2022).

The tourmaline crystal samples investigated were found, together with several other crystals, in a relatively large, flat, oblate pocket of ~80 dm^3 in volume (90 × 65 cm, up to 25 cm high), not affected by any weathering alteration, and in the core zone of the pegmatite body. The distribution of the minerals and the rock structures of this pocket reflect the typical asymmetric compositional and textural zoning of this dyke. The roof of the cavity was composed mostly of coarse-grained K-feldspar crystals, with quartz, minor albite, petalite and a few multicoloured tourmaline and pink beryl crystals. The floor of the cavity was mostly composed of medium-grained albite, with quartz, petalite, numerous multicoloured tourmaline crystals, and minor K-feldspar crystals and pollucite. Thin radial fractures penetrating from the miarolitic cavity into the surrounding pegmatite are evident in the Rosina pegmatite (Fig. 2), suggesting some phenomena of partial cavity collapse. As a result, we propose that the highly-reactive cavity fluids locally infiltrate these fractures, leading to late-stage corrosion and alteration of the previously-crystallised cavity-lining minerals. These processes are supported by the occurrence of fractured and decoloured biotite crystals, as well as altered spessartine garnet and petalite in the intermediate and lower border zone of the pegmatite (Fig. 2).

Experimental methods

Sample preparation

The crystal fragments (Fig. 1b) were glued to a glass slide using epoxy resin, with their length parallel to the surface of the slide.

https://doi.org/10.1180/mgm.2022.125 Published online by Cambridge University Press

Table 2. Representative compositions and atoms per formula unit (apfu) for the overgrowths OGY and OGZ in the tourmaline crystals studied from San Piero in Campo, Elba Island, Italy. Average values and data for representative analysed spots are reported.

	OGY			OGZ	
	spot #81	spot #84	Average $n = 8$	spot #73	Average $n = 4$
Length (μm)			~700		~1000
SiO_2 (wt.%)	37.32	38.18	37.78(34)	37.29	37.48(27)
TiO_2	0.07	0.02	0.04(4)	0.12	0.07(7)
B_2O_3 [a]	10.78	11.02	10.90	10.79	10.87
Al_2O_3	37.78	39.96	39.10(99)	38.25	39.33(93)
FeO_{tot}	0.48	0.12	0.20(19)	0.37	0.30(9)
MnO_{tot}	7.07	3.60	4.59(98)	5.86	4.31(95)
CaO	0.05	0.01	0.02(2)	0.02	0.01
Na_2O	2.31	2.49	2.44(9)	2.42	2.49(10)
Li_2O [c]	1.18	1.65	1.53	1.34	1.49
K_2O	0.01	–	0.01(1)	0.03	0.04(1)
F	0.15	0.06	0.11(4)	–	–
H_2O [a]	3.18	3.44	3.35	3.29	3.33
$-O \equiv F$	−0.06	−0.02	−0.05	–	–
MnO [d]	5.27	2.68	3.42	4.27	3.14
Mn_2O_3 [d]	2.00	1.02	1.30	1.77	1.30
Total	100.37	100.56	100.09	99.82	99.76
Atoms normalised to 31 anions					
Si (apfu)	5.997	6.024	6.023	6.004	5.995
Ti^{4+}	0.008	0.002	0.005	0.015	0.009
B	3.000	3.000	3.000	3.000	3.000
Al	7.180	7.430	7.345	7.260	7.414
Fe^{3+} [b]	0.065	0.016	0.027	0.049	0.040
Fe^{2+} [b]	–	–	–	–	–
Mn^{3+}	0.245	0.122	0.158	0.217	0.158
Mn^{2+}	0.720	0.358	0.462	0.583	0.426
Ca	0.008	0.002	0.004	0.003	0.002
Na	0.721	0.761	0.753	0.755	0.771
Li	0.765	1.047	0.981	0.868	0.958
K	0.002	–	0.002	0.006	0.008
F	0.076	0.029	0.055	–	–
OH	3.435	3.619	3.564	3.534	3.556

[a]Calculated by stoichiometry (see text)
[b]All Fe was considered to be Fe^{3+}, with the exception of the OGR overgrowth, based on the OAS results
[c]Estimated with the procedure of Pesquera *et al.* (2016)
[d]Determined by OAS
Errors for oxides and fluorine are standard deviations (in brackets); '–' indicates not detected.

A slice of each fragment was cut along the growth direction (crystallographic **c**-axis) and subsequently ground and polished to produce a flat surface with a uniform thickness of 500 μm for electron microprobe analysis (EMPA).

For spectroscopic analyses, fragments were glued to a glass slide using a thermoplastic resin and cut along the **c**-axis, as described above, with a thickness of ~1100 μm. Before analyses, slices were further thinned to a suitable thickness and doubly polished.

Electron microprobe analysis

Compositional data were collected along two traverses (A–B and C–D) parallel to the **c**-axis (Fig. 3). The first one (A–B) was conducted from the base to the termination of each crystal fragment, with an average step size of 800 μm, except for where it passed through the overgrowths, labelled as OGX, OGR and OGZ, where the step size was reduced to 130, 120 and 350 μm, respectively, to capture more fine-scale detail. A second short traverse (C–D), with a step size of 80 μm, was conducted to analyse a lateral overgrowth, labelled as OGY, and located on the prismatic section of the crystal. Electron microprobe analysis was undertaken using a CAMECA SX50 at the Istituto di Geologia Ambientale e Geoingegneria (CNR of Rome, Italy) operating in wavelength-dispersion mode with an accelerating potential of 15 kV, a sample current of 15 nA and a beam diameter of 10 μm. Eighty-seven spot analyses were collected. Minerals and synthetic compounds were used as reference materials as follows: wollastonite (Si, Ca); magnetite (Fe); rutile (Ti); corundum (Al); karelianite (V); fluorophlogopite (F); periclase (Mg); jadeite (Na); orthoclase (K); rhodonite (Mn); and metallic Cr. The PAP correction procedure for quantitative electron probe micro analysis was applied (Pouchou and Pichoir, 1991). Relative error on data was <5% and detection limits <0.03 wt.%.

Optical absorption spectroscopy

Polarised room-temperature optical absorption spectra of the overgrowths (OGX, OGR, OGY and OGZ) were obtained in the range of 35000–11000 cm^{-1} (286–909 nm) at a spectral resolution of 1 nm on doubly polished sections, using an AVASPEC-ULS2048×16 spectrometer attached via a 400 μm ultraviolet (UV) optical fibre cable to a Zeiss Axiotron UV-microscope. The diameter of the circular measure aperture was 50 μm. A 75 W xenon arc lamp was used as a light source and Zeiss Ultrafluar 10× lenses served as the objective and condenser. A UV-quality Glan-Thompson prism, with a working range from 40000 to 3704 cm^{-1} was used as a polariser. Data in the near infrared (NIR) range (11000–5000 cm^{-1}) were obtained at a spectral resolution of 4 cm^{-1} using a Bruker Vertex 70 spectrometer equipped with a halogen-lamp source and CaF_2 beam-splitter, coupled to a Hyperion 2000 IR-microscope equipped with a ZnSe wire-grid polariser and an InSb detector. The beam was collimated using an adjustable rectangular aperture with edges varying from 50–80 μm.

Determination of site populations

The wt.% of element oxides determined by EMPA were used to calculate the atomic fractions (atoms per formula unit, apfu). The B content was assumed to be stoichiometric (B = 3.00 apfu). Lithium was estimated using the procedure of Pesquera *et al.* (2016). The (OH) content was calculated by charge balance with the assumption (T + Y + Z) = 15.00 apfu and 31 anions (Tables 1, 2, 3 and 4).

On the basis of the apfu, the site populations (see 'Mineral formulae' below) for each overgrowth and prismatic section of the two tourmaline crystal fragments were calculated following the site allocation of ions recommended by Henry *et al.* (2011).

Results

Composition

Variations in composition for selected elements (in wt.%) along crystal traverses are shown in Fig. 3. Results reveal that each fragment is characterised by low Mn and Fe contents, except for the dark-coloured overgrowths (OGX, OGY, OGZ and OGR) where the MnO and FeO content increase sharply up to ~7 wt.% and 1 wt.%, respectively. The initial part of fragment I contains a slight enrichment in MnO, starting from a value of ~2 wt.% that progressively decreases below 0.3 wt.%, and then abruptly

https://doi.org/10.1180/mgm.2022.125 Published online by Cambridge University Press

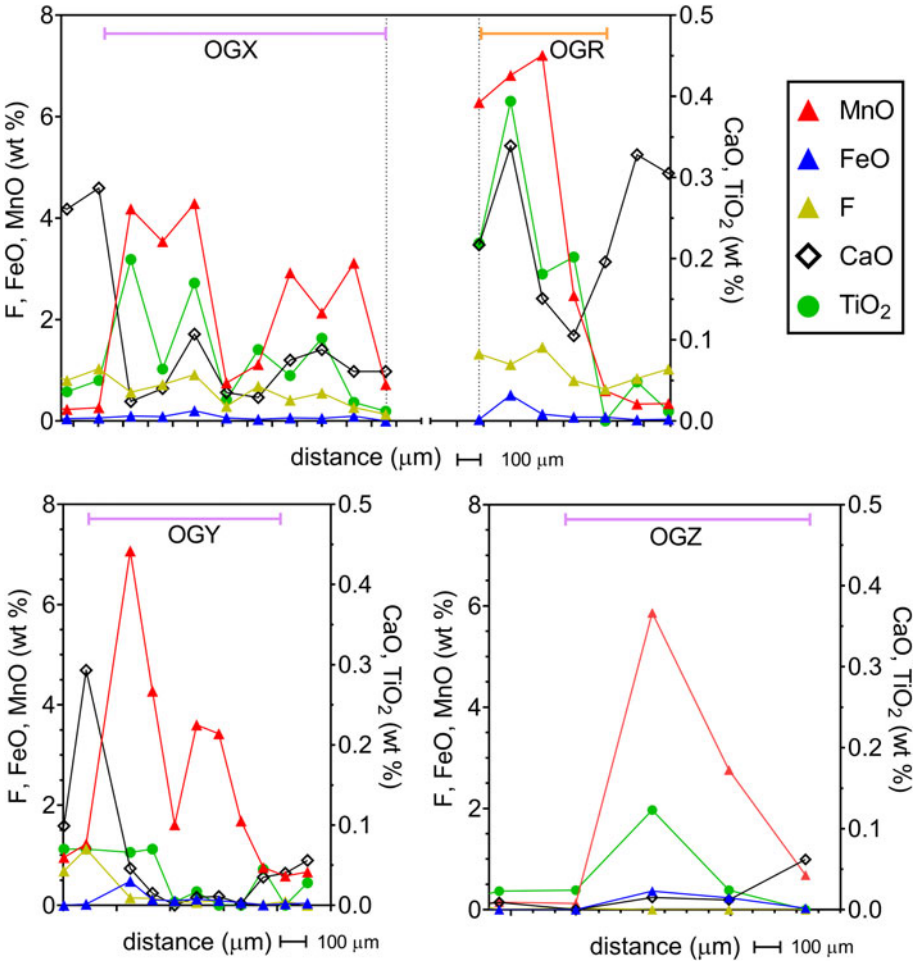

Fig. 4. Compositional analysis of all the overgrowths (OGX, OGR, OGY and OGZ) observable in the tourmaline crystal fragments. Scale bar = 100 μm.

increases at beginning of the OGX overgrowth. The variation in content of selected elements (in wt.%) along the overgrowths are given in Fig. 4. Vanadium, Cr and Mg were always below detection limits (<0.03 wt.%) in the samples investigated.

Compositions for selected representative spots analysed as well as the average values of each overgrowth (Tables 1, 2) and prismatic section (Tables 3, 4) of the two tourmaline crystal fragments are given in Tables 1–4. A full dataset from electron microprobe analysis for all samples analysed is available as Supplementary material. Note that in the overgrowths the oxidation state of Fe was assumed to be +3 as indicated by the presence of Mn^{3+} revealed by optical absorption spectroscopy (OAS), except for the OGR overgrowth, which contains Fe^{2+} (see below).

Compositional diagrams showing data from spot analysis relative to the prismatic section of fragment I and II, and the four different overgrowths are given in Fig. 5.

Mineral formulae

The resulting empirical formulae written in their ordered form, relative to average compositions of each overgrowth and prismatic section of the two tourmaline crystal fragments, as well as to selected representative spots analysed, are reported in Table 5.

All these compositions are consistent with a tourmaline belonging to the alkali-group, subgroup 2 (Henry *et al.*, 2011): they are Na-dominant at the X position of the general formula of tourmaline and hydroxy-dominant at W with $(OH+F)^- > O^{2-}$ and (OH) >> F, except for the OGR overgrowth and the prismatic section of fragment I, which are fluor-species as F > OH.

All the compositions are ^{Z}Al- and $^{Y}(Al_{1.5}Li_{1.5})$-dominant, and thus are elbaitic, $Na(Li_{1.5}Al_{1.5})Al_6Si_6O_{18}(BO_3)_3(OH)_3(OH,F)$, from a nomenclature viewpoint (Henry *et al.*, 2011). In particular, the overgrowths OGX, OGY and OGZ, can be classified as Mn-rich elbaite, whereas the overgrowth OGR is Mn-rich fluor-elbaite. Regarding the prismatic sections, fragments I and II correspond to fluor-elbaite and elbaite, respectively.

Optical absorption spectroscopy

Optical absorption spectra (**E⊥c** and **E||c**) recorded at selected spots within the differently coloured overgrowths are reported in Fig. 6. All the **E⊥c** spectra of the OGX, OGY and OGZ overgrowths display a main absorption band centred at ~18800 cm^{-1} and a weaker absorption band at ~22000 cm^{-1}. The spectrum of the OGX overgrowth recorded at spot 1 reveals additional absorption bands at ~24500 and ~9500 cm^{-1}. In contrast, the **E⊥c** spectrum recorded within the OGR overgrowth shows a different absorption pattern with two very broad bands at ~30700 and ~22700 cm^{-1}, and very weak bands at ~27000 and ~24500 cm^{-1}. Additional relatively weak and broad bands occur in the NIR region at ~9000 and ~14000 cm^{-1}. All the spectra recorded in light polarised parallel to the crystallographic **c**-axis (**E||c**), have a weaker absorption and additional very sharp bands between

https://doi.org/10.1180/mgm.2022.125 Published online by Cambridge University Press

Table 3. Representative compositions and atoms per formula unit (apfu) for fragment I, prismatic section of the tourmaline crystals studied from San Piero in Campo, Elba Island, Italy. Average values and data for representative analysed spots are reported.

	Prismatic section I		
	spot #2	spot #10	Average *n* = 12
SiO_2 (wt.%)	37.14	38.05	37.95(48)
TiO_2	0.09	0.04	0.05(3)
B_2O_3[a]	10.89	11.08	11.06
Al_2O_3	41.14	42.03	41.77(36)
FeO	0.01	–	0.03(3)
MnO	1.43	0.28	0.62(64)
CaO	0.47	0.27	0.34(8)
Na_2O	1.91	1.83	1.85(7)
Li_2O[b]	1.91	1.94	1.90
F	1.08	1.04	0.99(15)
H_2O[a]	3.00	3.20	3.18
–O ≡ F	–0.45	–0.44	–0.42
Total	98.49	99.33	99.35
Atoms normalised to 31 anions			
Si (apfu)	5.930	5.968	5.967
Ti^{4+}	0.011	0.004	0.006
B	3.000	3.000	3.000
Al	7.740	7.768	7.740
Fe^{2+}	0.001	–	0.003
Mn^{2+}	0.193	0.037	0.083
Ca	0.080	0.046	0.057
Na	0.591	0.556	0.563
Li	1.124	1.224	1.201
F	0.545	0.516	0.494
OH	3.193	3.344	3.334

[a]Calculated by stoichiometry (see text)
[b]Estimated with the procedure of Pesquera *et al.* (2016)
Errors for oxides and fluorine are standard deviations (in brackets); '–' indicates not detected.

Table 4. Representative compositions and atoms per formula unit (apfu) for fragment II, prismatic section of the tourmaline crystals studied from San Piero in Campo, Elba Island, Italy. Average values and data for representative analysed spots are reported.

	Prismatic section II					
	spot #28	spot #38	spot #40	spot # 58	spot #68	Average *n* = 49
SiO_2 (wt.%)	36.55	36.06	37.23	38.84	38.37	37.74(99)
TiO_2	0.01	–	0.04	–	0.01	0.02(2)
B_2O_3[a]	10.79	10.75	10.93	11.28	11.17	11.05
Al_2O_3	41.56	42.27	41.94	42.88	42.44	42.37(64)
FeO	0.04	0.01	–	–	0.01	0.02(2)
MnO	0.34	0.09	0.05	0.15	0.06	0.14(18)
CaO	0.31	0.01	0.02	0.01	–	0.07(11)
Na_2O	1.80	1.81	2.01	1.84	1.85	1.87(9)
Li_2O[b]	1.80	1.69	1.89	1.96	1.97	1.88
F	1.02	0.58	0.32	0.33	0.11	0.46(29)
H_2O[a]	3.08	3.25	3.50	3.64	3.75	3.46
–O ≡ F	–0.43	–0.24	–0.13	–0.14	–0.05	–0.19
Total	96.89	96.30	97.80	100.82	99.73	98.92
Atoms normalised to 31 anions						
Si (apfu)	5.889	5.830	5.919	5.983	5.970	5.935
Ti^{4+}	0.001	–	0.004	–	0.001	0.002
B	3.000	3.000	3.000	3.000	3.000	3.000
Al	7.890	8.057	7.860	7.784	7.782	7.852
Fe^{2+}	0.005	0.002	–	–	0.001	0.002
Mn^{2+}	0.047	0.012	0.006	0.019	0.008	0.019
Ca	0.053	0.002	0.004	0.001	–	0.012
Na	0.563	0.568	0.618	0.560	0.558	0.569
Li	1.166	1.099	1.209	1.214	1.233	1.189
F	0.521	0.295	0.160	0.160	0.056	0.227
OH	3.304	3.509	3.713	3.744	3.888	3.633

[a]Calculated by stoichiometry (see text)
[b]Estimated with the procedure of Pesquera *et al.* (2016)
Errors for oxides and fluorine are standard deviations (in brackets); '–' indicates not detected.

6700–7200 cm^{-1} in the NIR range ascribed to overtones of the fundamental (OH)-stretching modes.

Discussion

Composition analysis

The four overgrowths (OGX, OGR, OGY and OGZ) of the two tourmaline crystal fragments are characterised by a dark colour and a sudden increase in MnO, which rises up to 7 wt.%. In contrast, the prismatic section of fragment I and II has a very low MnO content, with the exception of the initial part of fragment I (up to 2 wt.%) (Fig. 3). Although the four overgrowths have similar composition, OGR has slightly more TiO_2, CaO and F, which increases, respectively, up to 0.40 wt.%, 0.35 wt.% and 1.2 wt.% (Fig. 4; Tables 1, 2). It should be noted that the overgrowths OGX, OGY and OGZ were formed in the direction of the analogous pole, whereas the overgrowth OGR was formed at the antilogous pole of fragment II. Although the Mn increase at the overgrowths is confirming a significant chemical evolution, the mineralogical species remain elbaite and F-elbaite. This compositional evolution trend is evident in the ternary plots of *X*- and *Y*-site occupancy (Fig. 5a,b), where overgrowths are characterised by an enrichment in Na and Mn, respectively. The increase in Mn at the overgrowths is consistent with the substitution of Li and Al at the *Y* site. A plot of content of 2Li *vs.* (Mn + Fe) at the *Y* site (Fig. 5c), confirms that the analysis points relating to the prismatic sections are close to an elbaite/F-elbaite composition. In contrast, data relating to the overgrowths are distributed along a trend line corresponding to a total or partial replacement of Li and Al with Mn/Fe. A plot of the content of F *vs.* Na (Fig. 5d) confirms the Na enrichment that characterises the overgrowths.

Furthermore, in many graphs it is possible to observe a different distribution of the data relating to the overgrowth at the antilogous pole (OGR) compared to the other overgrowths (OGX, OGY and OGZ). This different trend is particularly evident in the Ca *vs.* Ti plot (Fig. 5e), where most of the data points for the OGR overgrowth lie apart from the other ones. Interestingly, the data related to the different overgrowths follow a different compositional evolution trend in the ternary plot of Na/(Na + $^{X}\square$) *vs.* Mn/(Mn + 2Li) *vs.* F (Fig. 5f).

Comparison of the dark overgrowths

The dark overgrowths have been compared to ascertain if they were formed simultaneously in the same crystallisation environment. As stated above, all overgrowths are characterised by a comparable composition, which is consistent with their formation in the same environment. The antilogous overgrowth OGR compared to the analogous ones shows some differences in Ti, Ca and F content, as well as a smaller length (~500 μm for OGR, ~1000 μm for OGX and OGZ, and ~700 μm for the lateral overgrowth OGY) (Fig. 4; Tables 1, 2).

Additional evidence supporting the formation of the four overgrowths in the same crystallisation environment is provided by OAS data (Fig. 6). The overgrowth at the analogous poles (OGX, OGY and OGZ) share the same ~22000 and ~18800 cm^{-1}

https://doi.org/10.1180/mgm.2022.125 Published online by Cambridge University Press

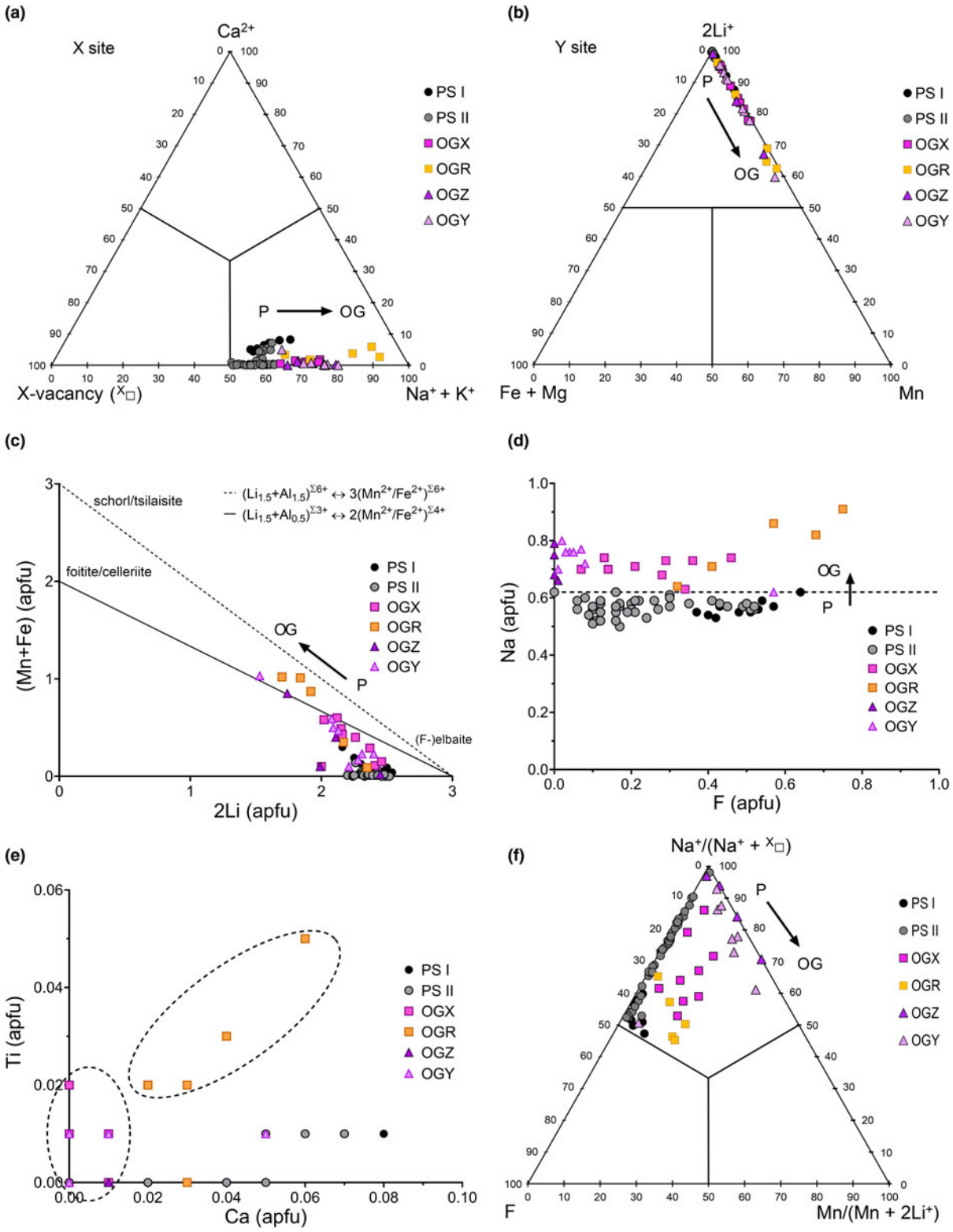

Fig. 5. Compositional diagrams determined by EMPA. Each point represents the result in apfu of a single spot analysis. The spot data for the different overgrowths (OGX, OGR, OGY and OGZ) and the prismatic sections of the two fragments (PS I and PS II) are distinguished by coloured labels. (a) *X*-site occupancy; (b) *Y*-site occupancy; (c) plot of 2Li *vs*. (Fe+Mn); (d) plot of F *vs*. Na; (e) plot of Ca *vs*. Ti; (f) ternary plot of Na/(Na + ^{X}□) *vs*. Mn/(Mn + 2Li) *vs*. F. Arrows highlight the compositional evolution trend from the prismatic section to the overgrowth. Dashed circles highlight the different distribution of the points relating to the overgrowth at the antilogous pole (OGR) compared to the other overgrowths (OGX, OGY and OGZ).

https://doi.org/10.1180/mgm.2022.125 Published online by Cambridge University Press

Table 5. Empirical formulae for the different overgrowths and prismatic sections of the tourmaline crystals investigated from San Piero Campo, Elba Island, Italy. Formulae relative to average compositions and for representative spots are reported.

Spots	Empirical chemical formulae
OGX (analogous pole of fragment I)[a]	
spot #13	$^{X}(Na_{0.73}\square_{0.27})_{\Sigma1.00}\ ^{Y}(Al_{1.39}Li_{1.01}Fe^{3+}_{0.01}Mn^{2+}_{0.37}Mn^{3+}_{0.20}Ti_{0.02})_{\Sigma3.00}\ ^{Z}Al_6[^{T}(Si_{5.99}Al_{0.01})O_{18}](BO_3)_3\ ^{V}(OH)_3\ ^{W}[(OH)_{0.54}F_{0.29}O_{0.17}]_{\Sigma1.00}$
spot #20	$^{X}(Na_{0.74}\square_{0.25}Ca_{0.01})_{\Sigma1.00}\ ^{Y}(Al_{1.47}Li_{1.08}Fe^{3+}_{0.01}Mn^{2+}_{0.27}Mn^{3+}_{0.15}Ti_{0.003})_{\Sigma2.98}\ ^{Z}Al_6(^{T}Si_{6.02}O_{18})(BO_3)_3\ ^{V}(OH)_3\ ^{W}[(OH)_{0.68}F_{0.13}O_{0.19}]_{\Sigma1.00}$
average (9 spots)	$^{X}(Na_{0.72}\square_{0.27}Ca_{0.01})_{\Sigma1.00}\ ^{Y}(Al_{1.42}Li_{1.09}Fe^{3+}_{0.01}Mn^{2+}_{0.29}Mn^{3+}_{0.16}Ti_{0.01})_{\Sigma2.98}\ ^{Z}Al_6(^{T}Si_{6.02}O_{18})(BO_3)_3\ ^{V}(OH)_3\ ^{W}[(OH)_{0.40}F_{0.29}O_{0.31}]_{\Sigma1.00}$
OGR (antilogous pole of fragment II)[a]	
spot #23	$^{X}(Na_{0.86}\square_{0.08}Ca_{0.06})_{\Sigma1.00}\ ^{Y}(Al_{0.94}Li_{0.92}Fe^{2+}_{0.08}Mn^{2+}_{0.94}Ti_{0.05})_{\Sigma2.93}\ ^{Z}Al_6\ ^{T}(Si_{6.07}O_{18})(BO_3)_3\ ^{V}(OH)_3\ ^{W}[(OH)_{0.17}F_{0.57}O_{0.26}]_{\Sigma1.00}$
average (5 spots)	$^{X}(Na_{0.82}\square_{0.14}Ca_{0.04})_{\Sigma1.00}\ ^{Y}(Al_{1.18}Li_{0.96}Fe^{2+}_{0.03}Mn^{2+}_{0.78}Ti_{0.03})_{\Sigma2.98}\ ^{Z}Al_6\ ^{T}(Si_{6.02}O_{18})(BO_3)_3\ ^{V}(OH)_3\ ^{W}[(OH)_{0.13}F_{0.60}O_{0.27}]_{\Sigma1.00}$
OGY (lateral overgrowth of fragment II)[a]	
spot #81	$^{X}(Na_{0.72}\square_{0.27}Ca_{0.01})_{\Sigma1.00}\ ^{Y}(Al_{1.18}Li_{0.77}Fe^{3+}_{0.07}Mn^{2+}_{0.72}Mn^{3+}_{0.25}Ti_{0.01})_{\Sigma3.00}\ ^{Z}Al_6\ ^{T}(Si_6O_{18})(BO_3)_3\ ^{V}(OH)_3\ ^{W}[(OH)_{0.44}F_{0.08}O_{0.48}]_{\Sigma1.00}$
spot #84	$^{X}(Na_{0.76}\square_{0.24})_{\Sigma1.00}\ ^{Y}(Al_{1.43}Li_{1.05}Fe^{3+}_{0.02}Mn^{2+}_{0.36}Mn^{3+}_{0.12}Ti_{0.002})_{\Sigma2.98}\ ^{Z}Al_6\ ^{T}(Si_{6.02}O_{18})(BO_3)_3\ ^{V}(OH)_3\ ^{W}[(OH)_{0.62}F_{0.03}O_{0.35}]_{\Sigma1.00}$
average (8 spots)	$^{X}(Na_{0.76}\square_{0.24})_{\Sigma1.00}\ ^{Y}(Al_{1.35}Li_{0.98}Fe^{3+}_{0.03}Mn^{2+}_{0.46}Mn^{3+}_{0.16}Ti_{0.01})_{\Sigma2.99}\ ^{Z}Al_6\ ^{T}(Si_{6.01}O_{18})(BO_3)_3\ ^{V}(OH)_3\ ^{W}[(OH)_{0.56}F_{0.06}O_{0.38}]_{\Sigma1.00}$
OGZ (analogous pole of fragment II)[a]	
spot #73	$^{X}(Na_{0.76}K_{0.01}\square_{0.23})_{\Sigma1.00}\ ^{Y}(Al_{1.26}Li_{0.87}Fe^{3+}_{0.05}Mn^{2+}_{0.58}Mn^{3+}_{0.22}Ti_{0.02})_{\Sigma3.00}\ ^{Z}Al_6\ ^{T}(Si_{6.00}O_{18})(BO_3)_3\ ^{V}(OH)_3\ ^{W}[(OH)_{0.53}O_{0.47}]_{\Sigma1.00}$
average (4 spots)	$^{X}(Na_{0.77}K_{0.01}\square_{0.22})_{\Sigma1.00}\ ^{Y}(Al_{1.41}Li_{0.96}Fe^{3+}_{0.03}Mn^{2+}_{0.43}Mn^{3+}_{0.16}Ti_{0.01})_{\Sigma3.00}\ ^{Z}Al_6\ ^{T}(Si_6O_{18})(BO_3)_3\ ^{V}(OH)_3\ ^{W}[(OH)_{0.56}O_{0.44}]_{\Sigma1.00}$
Prismatic section of fragment I	
spot #2	$^{X}(Na_{0.59}\square_{0.33}Ca_{0.08})_{\Sigma1.00}\ ^{Y}(Al_{1.67}Li_{1.12}Mn^{2+}_{0.19}Ti_{0.01})_{\Sigma2.99}\ ^{Z}Al_6[^{T}(Si_{5.93}Al_{0.07})_{\Sigma6.00}O_{18}](BO_3)_3\ ^{V}(OH)_3\ ^{W}[(OH)_{0.19}F_{0.54}O_{0.27}]_{\Sigma1.00}$
spot #10	$^{X}(Na_{0.56}\square_{0.39}Ca_{0.05})_{\Sigma1.00}\ ^{Y}(Al_{1.74}Li_{1.22}Mn^{2+}_{0.04}Ti_{0.004})_{\Sigma3.00}\ ^{Z}Al_6[^{T}(Si_{5.97}Al_{0.03})_{\Sigma6.00}O_{18}](BO_3)_3\ ^{V}(OH)_3\ ^{W}[(OH)_{0.34}F_{0.52}O_{0.14}]_{\Sigma1.00}$
average (12 spots)	$^{X}(Na_{0.56}\square_{0.38}Ca_{0.06})_{\Sigma1.00}\ ^{Y}(Al_{1.71}Li_{1.20}Mn^{2+}_{0.08}Ti_{0.01})_{\Sigma3.00}\ ^{Z}Al_6[^{T}(Si_{5.97}Al_{0.03})_{\Sigma6.00}O_{18}](BO_3)_3\ ^{V}(OH)_3\ ^{W}[(OH)_{0.33}F_{0.49}O_{0.18}]_{\Sigma1.00}$
Prismatic section of fragment II	
spot #28	$^{X}(Na_{0.56}\square_{0.39}Ca_{0.05})_{\Sigma1.00}\ ^{Y}(Al_{1.78}Li_{1.17}Mn^{2+}_{0.05})_{\Sigma3.00}\ ^{Z}Al_6[^{T}(Si_{5.89}Al_{0.11})_{\Sigma6.00}O_{18}](BO_3)_3\ ^{V}(OH)_3\ ^{W}[(OH)_{0.30}F_{0.52}O_{0.18}]_{\Sigma1.00}$
spot #38	$^{X}(Na_{0.57}\square_{0.43})_{\Sigma1.00}\ ^{Y}(Al_{1.89}Li_{1.10}Mn^{2+}_{0.01})_{\Sigma3.00}\ ^{Z}Al_6[^{T}(Si_{5.83}Al_{0.17})_{\Sigma6.00}O_{18}](BO_3)_3\ ^{V}(OH)_3\ ^{W}[(OH)_{0.51}F_{0.30}O_{0.19}]_{\Sigma1.00}$
spot #40	$^{X}(Na_{0.62}\square_{0.38})_{\Sigma1.00}\ ^{Y}(Al_{1.78}Li_{1.21}Mn^{2+}_{0.01})_{\Sigma3.00}\ ^{Z}Al_6[^{T}(Si_{5.92}Al_{0.08})_{\Sigma6.00}O_{18}](BO_3)_3\ ^{V}(OH)_3\ ^{W}[(OH)_{0.71}F_{0.16}O_{0.13}]_{\Sigma1.00}$
spot #58	$^{X}(Na_{0.56}\square_{0.44})_{\Sigma1.00}\ ^{Y}(Al_{1.76}Li_{1.21}Mn^{2+}_{0.02})_{\Sigma3.00}\ ^{Z}Al_6[^{T}(Si_{5.98}Al_{0.02})_{\Sigma6.00}O_{18}](BO_3)_3\ ^{V}(OH)_3\ ^{W}[(OH)_{0.74}F_{0.16}O_{0.10}]_{\Sigma1.00}$
spot #68	$^{X}(Na_{0.56}\square_{0.44})_{\Sigma1.00}\ ^{Y}(Al_{1.75}Li_{1.23}Mn^{2+}_{0.01})_{\Sigma2.98}\ ^{Z}Al_6[^{T}(Si_{5.97}Al_{0.03})_{\Sigma6.00}O_{18}](BO_3)_3\ ^{V}(OH)_3\ ^{W}[(OH)_{0.89}F_{0.06}O_{0.05}]_{\Sigma1.00}$
average (49 spots)	$^{X}(Na_{0.57}\square_{0.42}Ca_{0.01})_{\Sigma1.00}\ ^{Y}(Al_{1.79}Li_{1.19}Mn^{2+}_{0.02})_{\Sigma3.00}\ ^{Z}Al_6[^{T}(Si_{5.94}Al_{0.06})_{\Sigma6.00}O_{18}](BO_3)_3\ ^{V}(OH)_3\ ^{W}[(OH)_{0.63}F_{0.23}O_{0.14}]_{\Sigma1.00}$

[a]Empirical formulae were based on the Mn_2O_3 content calculated by OAS data.

absorption bands that can be assigned to Mn^{3+} *d–d* transitions (Reinitz and Rossman, 1988; Taran *et al.*, 1993; Ertl *et al.*, 2005; Bosi *et al.*, 2021). The additional bands at ~9500 and ~24500 cm^{-1} observed in the spectrum recorded at spot 1 of the OGX overgrowth can be ascribed to a Mn^{3+} spin-allowed *d–d* transition and a Mn^{2+} spin-forbidden transition, respectively (Bosi *et al.*, 2021). These assignments agree with the observed purplish-red colour of these overgrowths, mainly ascribed to the presence of Mn^{3+} as chromophore (Pezzotta and Laurs, 2011). On the basis of the intensity of the Mn^{3+} band at ~18800 cm^{-1} in the spectra perpendicular to the **c**-axis of the analogous overgrowths OGX, OGY and OGZ (Fig. 6), and using the molar extinction coefficient suggested by Reinitz and Rossman (1988), the Mn_2O_3 content in these overgrowths was calculated (Table 6). The top of the overgrowths OGX, OGY and OGZ are characterised by the same contents of Mn_2O_3 (1.3 wt.%) with a Mn^{3+}/Mn_{tot} ratio ranging from 0.27 to 0.39. This observation, together with the similar composition, is consistent with overgrowths formed simultaneously in the crystallisation environment. It should be noted that a second OAS analysis on the bottom part of the OGX overgrowth (spot 1), revealed a greater amount of Mn_2O_3 (2.93 wt.%) and a higher Mn^{3+}/Mn_{tot} ratio. The presence of Mn^{3+} suggests an oxidising environment during the crystallisation of the overgrowths.

The optical absorption spectra of the OGR overgrowth revealed only the presence of very weak Mn^{2+} spin-forbidden bands (~27000 and ~24500 cm^{-1}), in addition to strong and very broad bands at ~30700 and ~22700 cm^{-1}, which are caused by Mn^{2+}–Ti^{4+} and Fe^{2+}–Ti^{4+} IVCT (Intervalence Charge Transfer) transitions, respectively (Rossman and Mattson, 1986; Taran *et al.*, 1993). The latter two are consistent with compositional data, which revealed an increased amount of Ti in the OGR overgrowth compared to the other ones. The broad and moderately intense bands in the NIR region at ~9000 and ~14000 cm^{-1}, which are caused by spin-allowed transitions in Fe^{2+} (Mattson and Rossman, 1987) do not contribute to the colour of the samples. The band assignments for the OGR overgrowth agree with its yellow–orange colouration due to the presence of Mn^{2+} and Mn^{2+}–Ti^{4+} IVCT as chromophores (Rossman and Mattson, 1986; Laurs *et al.*, 2007; Pezzotta and Laurs, 2011). Considering the comparable total MnO contents of all the dark-coloured overgrowths (~4.5 wt.%), and that OGZ, OGY and OGR belong to the same crystal fragment and therefore grew at the same

Table 6. Summary of the OAS results for selected data points on the overgrowths including observed absorption bands, total content of MnO and relative amount of Mn^{3+} calculated by the molar extinction coefficient.

Absorption band	Assignment	OGX spot 1	OGX spot 2	OGY	OGZ	OGR
~30700 cm^{-1}	Mn^{2+}–Ti^{4+} IVCT transition					+
~27000 cm^{-1}	Mn^{2+} spin-forbidden transition					+
~24500 cm^{-1}	Mn^{2+} spin-forbidden transition	+				+
~22700 cm^{-1}	Fe^{2+}–Ti^{4+} IVCT transition					+
~22000 cm^{-1}	Mn^{3+} *d–d* transition	+	+	+	+	
~18800 cm^{-1}	Mn^{3+} *d–d* transition	+	+	+	+	
~14000 cm^{-1}	Fe^{2+} *d–d* transition					+
~9500 cm^{-1}	Mn^{3+} *d–d* transition	+				
~9000 cm^{-1}	Fe^{2+} *d–d* transition					+
MnO_{tot} (wt.%)#		4.18	3.11	3.51	4.31	6.76
Mn_2O_3 (wt.%)*		2.93	1.34	1.30	1.30	0
Mn^{3+}/Mn_{tot}		0.63	0.39	0.33	0.27	0

+Absorption band present

#MnO_{tot} content at the OAS spot was determined on the basis of the chemical analysis conducted along the considered traverses

*Calculated considering the intensity of the Mn^{3+} band at 18800 cm^{-1} in **E⊥c** spectra, in combination with the molar extinction coefficient of 7.5 for that absorption band (suggested by Reinitz and Rossman, 1988). Values of absorber thickness: OGX = 820 μm; OGY = 902 μm; OGZ = 658 μm; OGR = 437 μm.

https://doi.org/10.1180/mgm.2022.125 Published online by Cambridge University Press

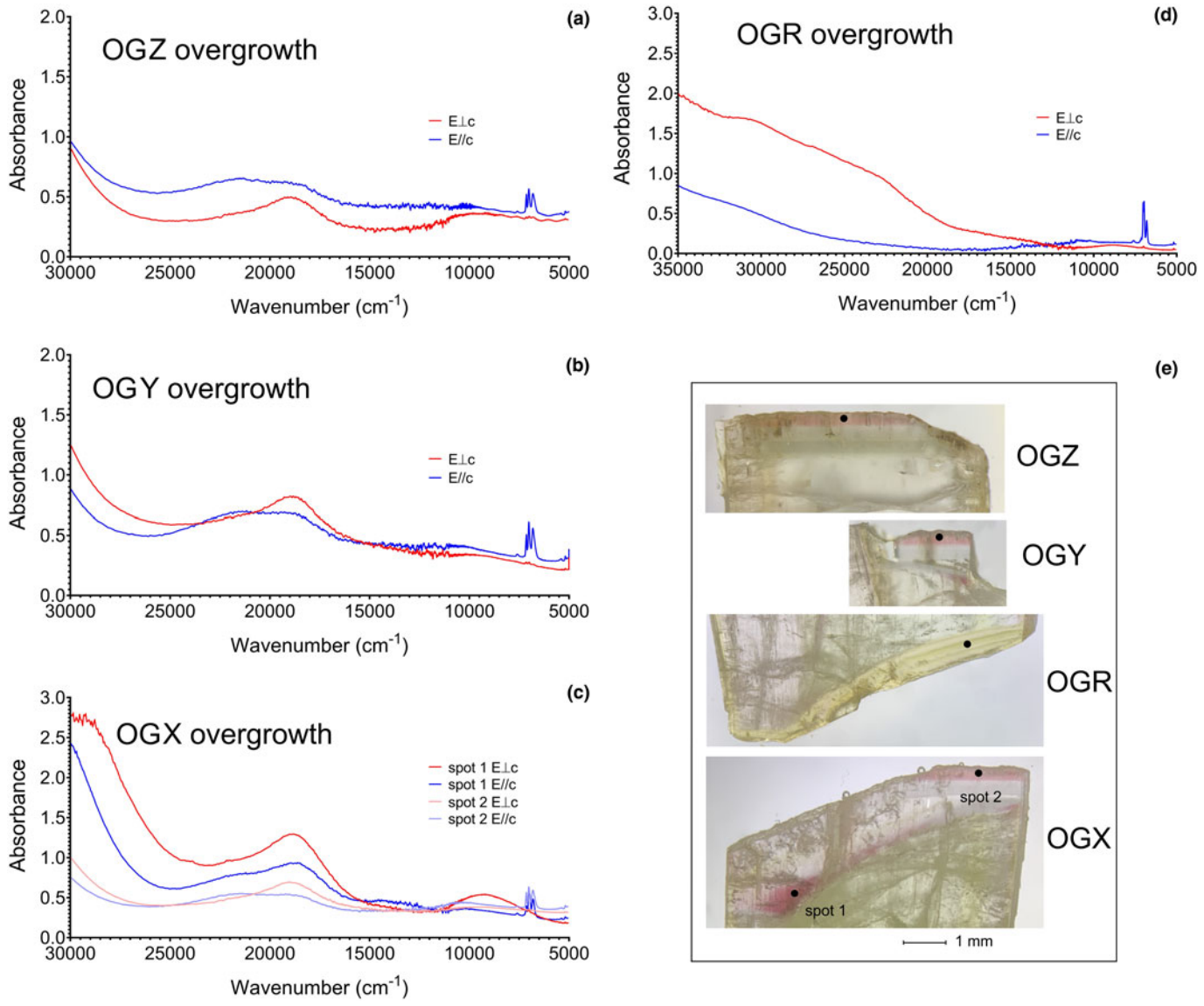

Fig. 6. Optical adsorption spectra for the dark coloured overgrowths polarised perpendicular (**E⊥c**) and parallel (**E||c**) to the **c**-axis direction of selected spots in the (a) OGZ, (b) OGY, (c) OGX and (d) OGR overgrowths. (e) Optical microscopy images of the OGX, OGR, OGY and OGZ overgrowths. The location of spots used for OAS are indicated. Sample thickness: OGX = 820 μm; OGY = 902 μm; OGZ = 658 μm; OGR = 437 μm. Scale bar = 1 mm.

time, the absence of Mn^{3+} *d*–*d* transitions in the OGR spectra suggests a strong preferential incorporation of Mn^{2+} ions in the antilogous overgrowth, even in the presence of Mn^{3+} in the crystallisation environment. A similar crystal-chemical behaviour is observed for Ti, Ca and F, which are preferentially incorporated at the antilogous pole (Fig. 4; Table 1). As a result, the antilogous pole shows a different growth history, with a preferential incorporation of Ca, F and Ti, as well as a selective uptake of Mn^{2+} over Mn^{3+}, leading to a different colouration and tourmaline species (fluor-elbaite instead of elbaite, typical of the other overgrowths). This different behaviour is also evident in several compositional diagrams, where OGR data points occupy a different position in the plot compared to the other overgrowths (Fig. 5).

The differences observed in the composition and spectroscopic analysis between the analogous and antilogous overgrowths can be related to differences in the growth process occurring at the two poles (surface energy, nucleation speed, piezo- and pyro-electrical properties) (Henry and Dutrow, 1992).

The formation of the dark-coloured overgrowths is probably the result of a pocket rupture. This event changed the chemical environment within the pocket, leading to a sudden increase in the availability of Mn in the geochemical system. Although the initial part of the fragment exhibits a slight enrichment in MnO (up to 2 wt.%), this is related to the amount of Mn remaining available in the pegmatitic system after the early crystallisation of spessartine. The subsequent progressive decrease in MnO content in fragment I is the result of Mn depletion in the system due to tourmaline crystallisation. Spessartine crystallisation is recognised as an important mechanism for regulating the Mn content during the evolution of the pegmatite systems (Novák *et al.*, 2000; Laurs *et al.*, 2007) and, in Elba pegmatites, spessartine garnet represents the main competitor for Mn during the evolution of the pegmatite system (Bosi *et al.*, 2022). Indeed, spessartine garnet

https://doi.org/10.1180/mgm.2022.125 Published online by Cambridge University Press

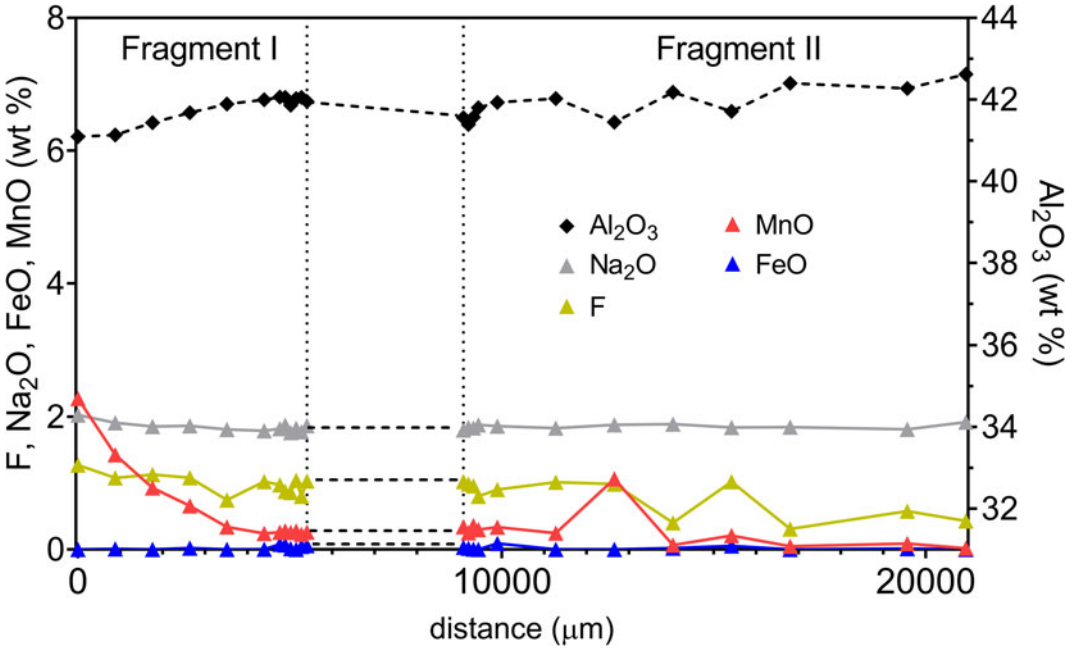

Fig. 7. Compositional analysis of the two prismatic sections close to the OGX/OGR breakage.

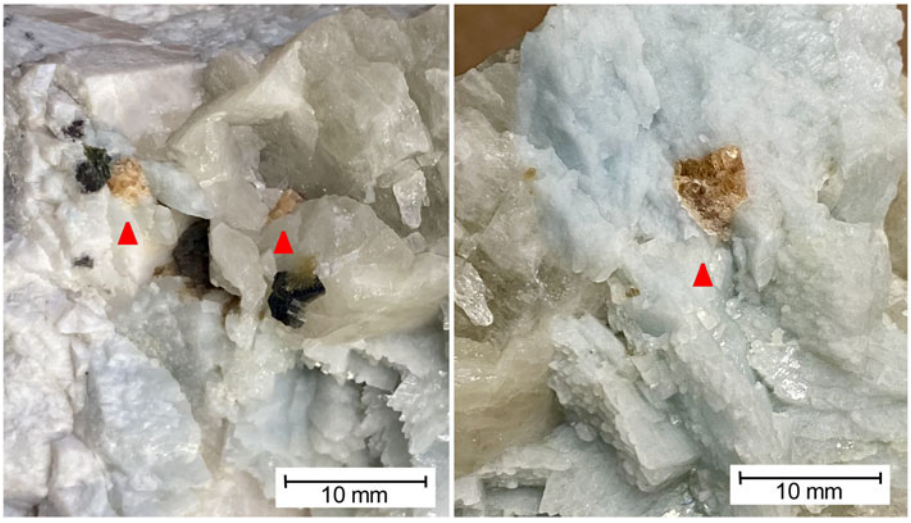

Fig. 8. Examples of extensively fractured and partially corroded spessartine crystals (red arrows) 'frozen' in quartz and feldspars in proximity of cavities of the Rosina pegmatite. Crystals up to 6 mm in diameter. Scale bar = 10 mm.

in the Rosina pegmatite is present in the intermediate zone of the pegmatite, close to the miarolitic cavity (Fig. 2).

The very limited amount of Fe in the OGR overgrowth, in addition to limited amounts in all the other overgrowths, led us to exclude that this may represent the root part of the crystal. Therefore, it is reasonable to assume that this dark termination was formed on a new growth surface as a consequence of a natural breakage event which the prismatic section of the crystal underwent. Observing the two crystal fragments and disregarding the dark-coloured overgrowths, the shape of the analogous termination of fragment I and the antilogous one of fragment II match perfectly. This demonstrates that they are two crystal fragments belonging to the same original tourmaline crystal which broke during pocket collapse and on which late-stage overgrowths (OGX and OGR) occurred.

Comparison of the prismatic sections

In support of the evidence that the fragments (I and II) were part of the same original crystal, the analytical data document a perfect continuity (Fig. 7). Disregarding the data points related to the OGX and OGR overgrowths, compositional analysis revealed no significant variations for the different oxide components between the two prismatic sections, as expected if they had been joined (Fig. 7; Tables 3, 4). As consequence of the crystal breakage, OGX and OGR overgrowths have been formed on the new growth surfaces generated by the break.

Genetic model for the dark-coloured overgrowths

Elba tourmalines are renowned all over the world for their characteristic dark terminations, which are due to the incorporation of

https://doi.org/10.1180/mgm.2022.125 Published online by Cambridge University Press

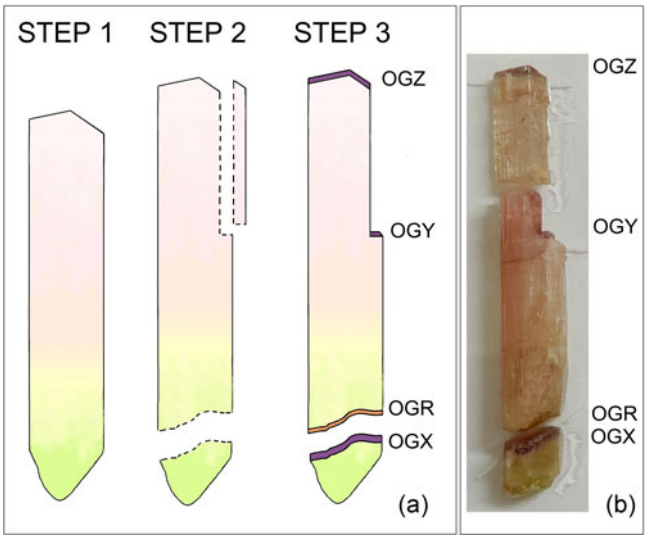

Fig. 9. Schematic representation of the history of growth of the tourmaline crystals investigated. (a) Step 1: tourmaline crystal growth from light green to pale pink in the direction of the analogous pole (**c**$^-$ side). Step 2: breakage of the crystal as a result of the pocket rupture event followed by changes in the composition of the crystallisation environment. Step 3: generation of late-stage dark-coloured overgrowths at the analogous (OGX, OGY, OGZ) and at the antilogous (OGR) poles in a Mn-rich environment. (b) Image of the tourmaline crystals investigated.

elements, such as Fe and/or Mn during the latest stages of crystallisation in miarolitic cavities (Pezzotta, 2021). However, the mechanisms that led to the availability of these elements in the residual fluids have previously been unclear.

Microstructural and paragenetic observations of the cavities in which tourmaline crystals with dark-coloured overgrowths were formed, provide evidence that such pockets are characterised by: (1) thin fractures penetrating from the cavity into the enclosing pegmatite; (2) leaching and corrosion of early-formed cavity-lining and cavity-coating Fe- and Mn-rich minerals crosscut by the fractures; (3) partial collapse of quartz and feldspar crystal aggregates; and (4) the breakage of some tourmaline crystals as a consequence of a partial pocket collapse (Bosi *et al.*, 2022; Altieri *et al.*, 2022). These features are particularly evident in the Rosina pegmatite from which the tourmaline crystals originated (Fig. 2). The pocket rupture occurred during the formation of a series of fractures penetrating the surrounding pegmatite, in which more primitive accessory minerals such as spessartine garnet and Fe-rich mica crystals were present (Fig. 2). Highly-reactive late-stage cavity fluids penetrating the fractures, allowed the corrosion of the Fe- and Mn-rich minerals causing a sudden change in the composition of the pocket crystallisation environment. Etching of spessartine garnet by late-stage reactive fluids has already been reported by London (2006) and Felch *et al.* (2016), and similar evidence of corroded spessartine crystals occurs in the Rosina pegmatite (Fig. 8). To account for the presence of Mn both in +2 and +3 redox states in the dark-coloured overgrowths, corrosion and alteration phenomena probably occurred in a relatively oxidising environment.

The pocket rupture was responsible for the breakage of the crystal investigated resulting in the formation of two new growth surfaces (OGX and OGR). In our model, OGZ represents the overgrowth at the termination of the original analogous pole of the crystal, whereas OGX and OGR correspond to the overgrowths formed at the new analogous and antilogous pole surfaces, respectively, as a result of the crystal breakage. The OGY overgrowth is related to a smaller lateral crystal breakage (Fig. 9).

The crystal breakage strengthens the hypothesis that the cavity has undergone a mechanical destabilisation. Consequently, the tourmaline crystal fragments preserved important records not only in terms of compositional variations of the geochemical system represented by the dark overgrowths, but also in the mechanical events, i.e. the crystal breakage.

A comparison of the overgrowths at the analogous and antilogous poles provides evidence of a preferential incorporation of particular elements at growth surfaces. The antilogous pole relative to the analogous pole is characterised by a different growth rate and higher concentrations of Ca, F and Ti. The differential uptake of these elements at these poles have been described by Henry and Dutrow (1992) and van Hinsberg *et al.* (2006) as a result of a combined effect of "lattice site morphology" on the different growth faces and dipolar surface charge which is related to the systematic orientation of the ring of tetrahedra. Here we report a further preference at the level of the ionic charge of the same elements. OAS data show a selective uptake of Mn^{2+} at the antilogous pole in the presence of a substantial amount of Mn^{3+} ions that preferred the analogous one. This differential uptake has never been reported previously and could be related to a greater partition coefficient for Mn^{3+} at the analogous surface. The preferential uptake of Mn^{3+} ions by the analogous growth surfaces led to a decrease in the Mn^{3+}/Mn_{tot} ratio in the crystallising fluids. The change in this ratio can be deduced by analysing the OAS data of the more extended OGX overgrowth which is characterised by a marked decrease in Mn^{3+} content along the growth direction, maintaining approximately the same MnO_{tot} content.

Conclusions

The tourmaline crystal fragments analysed illustrate the mechanical and compositional changes during the latest stages of cavity evolution as a consequence of a pocket rupture event. The comparison of the dark overgrowths formed on the direction of the analogous pole and the antilogous one in the same crystal, has provided new evidence regarding the different growing process occurring at the two poles involving Mn^{2+}/Mn^{3+} ions.

This work clearly correlates structural information, i.e. fracturing of the pocket and breakage of tourmaline crystals, to late-stage tourmaline growth, and permitted definition of a genetic model for the dark-coloured overgrowths in Elba tourmaline crystals.

Acknowledgements. Sample preparation for chemical and spectroscopic analyses was carried out with the support of Dr. D. Mannetta to whom the authors express their gratitude. The authors thank M. Serracino for his assistance during chemical analyses. F.B. acknowledges funding by Sapienza University of Rome (Prog. Università 2020) and by the Italian Ministry of Education (MIUR)–PRIN 2020, ref. 2020WYL4NY. The authors thank Jan Cempírek and an anonymous reviewer for their constructive comments that helped to improve the manuscript and Principal Editor Roger Mitchell for editorial assistance.

Supplementary material. To view supplementary material for this article, please visit https://doi.org/10.1180/mgm.2022.125

Competing interests. The authors declare none.

References

Agrosì, G., Bosi, F., Lucchesi, S., Melchiorre, G. and Scandale, E. (2006) Mn-tourmaline crystals from island of Elba (Italy): Growth history and growth marks. *American Mineralogist*, **91**, 944–952.

Altieri A., Pezzotta F., Skogby H., Hålenius U. and Bosi, F. (2022) Blue-growth zones caused by Fe^{2+} in tourmaline crystals from the San Piero in Campo gem-bearing pegmatites, Elba Island, Italy. *Mineralogical Magazine*, **86**, 910–919. https://doi.org/10.1180/mgm.2022.101.

Aurisicchio C., Ottolini L. and Pezzotta F. (1999): Electron- and ion-microprobe analyses, and genetic inferences of tourmalines of the foitite–schorl solid solution, Elba Island (Italy). *European Journal of Mineralogy*, **11**, 217–225.

Bosi F. (2018) Tourmaline crystal chemistry. *American Mineralogist*, **103**, 2, 298–306.

Bosi F., Celata B., Skogby H., Hålenius U., Tempesta G., Ciriotti M.E., Bittarello E., and Marengo A. (2021) Mn-bearing purplish-red tourmaline from the Anjanabonoina pegmatite, Madagascar. *Mineralogical Magazine*, **85**, 242–253.

Bosi F., Pezzotta F., Altieri A., Andreozzi G.B., Ballirano P., Tempesta G., Cempírek J., Škoda R., Filip J., Čopjacová R., Novák M., Kampf A.R., Scribner E.D., Groat L.A. and Evans R.J. (2022) Celleriite, $\square(Mn_2^{2+}Al)Al_6(Si_6O_{18})(BO_3)_3(OH)_3(OH)$, a new mineral species of the tourmaline supergroup. *American Mineralogist*, **107**, 31–42.

Buřival Z. and Novák M. (2015) Hydrothermal replacement of garnet by tourmaline in elbaite subtype LCT pegmatites. 7th *International Symposium on Granitic Pegmatites, PEG* 2015 *Książ, Poland*.

Černý P. (2000) Constitution, petrology, affiliations and categories of miarolitic pegmatites. *Memorie della Società Italiana di Scienze Naturali e del Museo Civico di Storia Naturale di Milano*, **30**, 5–12

Dutrow B.L. and Henry D.J. (2000) Complexly zoned fibrous tourmaline, Cruzeiro mine, Minas Gerais, Brazil: a record of evolving magmatic and hydrothermal fluids. *The Canadian Mineralogist*, **38**, 131–143.

Dutrow B.L. and Henry D.J. (2011) Tourmaline: A geologic DVD. *Elements*, **7**, 301–306.

Dutrow B.L. and Henry D.J. (2016) Fibrous tourmaline: a sensitive probe of fluid compositions and petrologic environments. *The Canadian Mineralogist*, **54**, 311–335.

Dutrow B.L. and Henry D.J. (2018) Tourmaline compositions and textures: reflections of the fluid phase. *Journal of Geosciences*, **63**, 99–110.

Ertl A., Rossman G.R., Hughes J.M., Prowatke S. and Ludwig T. (2005) Mn-bearing "oxy-rossmanite" with tetrahedrally coordinated Al and B from Austria: Structure, chemistry and infrared and optical spectroscopic study. *American Mineralogist*, **90**, 481–487.

Felch. M., Falster A.U., and Simmons W.B. (2016) Iron-bearing pollucite and tourmaline replacement of garnet in the garnet line in the Mt. Mica and Havey pegmatites, Western Maine. *The Canadian Mineralogist*, **54**, 1071–1086.

Foord E.E. (1976) *Mineralogy and Petrogenesis of Layered Pegmatite–Aplite Dikes in the Mesa Grande District, San Diego County, California*. Ph.D. thesis, Stanford University, Stanford, California.

Hawthorne F.C. and Dirlam D.M. (2011) Tourmaline the indicator mineral: From atomic arrangement to Viking navigation. *Elements*, **7**, 307–312.

Henry D.J. and Dutrow B.L. (1992) Tourmaline in a low grade clastic metasedimentary rocks: an example of the petrogenetic potential of tourmaline. *Contributions to Mineralogy and Petrology*, **112**, 203–218.

Henry D.J. and Dutrow B.L. (2018) Tourmaline studies through time: contributions to scientific advancements. *Journal of Geosciences*, **63**, 77–98.

Henry D.J., Novák M., Hawthorne F.C., Ertl A., Dutrow B., Uher P. and Pezzotta F. (2011) Nomenclature of the tourmaline supergroup minerals. *American Mineralogist*, **96**, 895–913.

Laurs B.M., Simmons W.B., Rossman G.R., Fritz E.A, Koivula J.I., Anckar B. and Falster A.U. (2007) Yellow Mn-rich tourmaline from the Canary Mining Area, Zambia. *Gems & Gemology*, **43**, 314–331.

London, D. (2006) *Spessartine from Navegador, Minas Gerais, Brazil: etch or growth features*. http://www.minsocam.org/msa/special/pig/pig_articles/etched_spssrtn.pdf

Mattson S.M. and Rossman G.R. (1987) Fe^{2+}-Fe^{3+} interactions in tourmaline. *Physics and Chemistry of Minerals*, **14**, 163–171.

Novák M. and Taylor M.C. (2000) Foitite: formation during late stages of evolution of complex granitic pegmatites at Dobrá Voda, Czech Republic, and Pala, California, U.S.A. *The Canadian Mineralogist*, **38**, 1399–1408.

Novák M., Selway J.B., Černý P., Chapman R.C. and Masau M. (2000) Correlation between Mn content in tourmaline and garnet abundance in two elbaite-subtype pegmatites: Dolní Rožínka and Pikárec, Czech Republic. *Geological Association of Canada - Mineralogical Association of Canada, Joint Annual Meeting*, abstract #584.

Orlandi P. and Pezzotta F. (1996) *Minerali dell'Isola d'Elba, i minerali dei giacimenti metalliferi dell'Elba orientale e delle pegmatiti del M.te Capanne*. Ed. Novecento Grafico, Bergamo, Italy 248 pp.

Pesquera A., Gil-Crespo P.P, Torres-Ruiz F., Torres-Ruiz J. and Roda-Robles E. (2016) A multiple regression method for estimating Li in tourmaline from electron microprobe analyses. *Mineralogical Magazine*, **80**, 1129–1133.

Pezzotta F. (2000) Internal structures, parageneses and classification of the miarolitic (Li-bearing) complex pegmatites of Elba Island (Italy). *Memorie della Società Italiana di Scienze Naturali e del Museo Civico di Storia Naturale di Milano*, **30**, 29–43.

Pezzotta F. (2021) A history of tourmaline from the Island of Elba. *The Mineralogical Record*, **52**, 669–720.

Pezzotta F. and Laurs B.M. (2011) Tourmaline: The kaleidoscopic gemstone. *Elements*, **7**, 331–336.

Pouchou J.L. and Pichoir F. (1991) Quantitative analysis of homogeneous or stratified microvolumes applying the model "PAP". Pp. 31–75 in: *Electron Probe Quantitation* (K.F.J. Heinrich and D.E. Newbury, editors). Plenum, New York.

Reinitz I. and Rossman G.R. (1988) Role of natural radiation in tourmaline colouration. *American Mineralogist*, **73**, 822–825.

Rossman G.R. and Mattson S.M. (1986) Yellow, Mn-rich elbaite with Mn-Ti intervalence charge transfer. *American Mineralogist*, **71**, 599–602.

Selway J.B. (1999) *Compositional Evolution of Tourmaline in Granitic Pegmatites*. Ph.D. thesis, University Manitoba, Winnipeg, Manitoba, USA.

Taran M.N., Lebedev A.S. and Platonov A.N. (1993) Optical absorption spectroscopy of synthetic tourmalines. *Physics and Chemistry of Minerals*, **20**, 209–220.

Trevisan L. (1951) La 55a Riunione Estiva della Società Geologica Italiana. *Isola d'Elba, Settembre* 1951. *Bollettino della Società Geologica Italiana*, **70**(1953), 435–472.

van Hinsberg V.J., Schumacher J.C., Kearns, S., Mason P.R.D. and Franz G. (2006) Hourglass sector zoning in metamorphic tourmaline and resultant major and trace-element fractionation. *American Mineralogist*, **91**, 717–728.

van Hinsberg V.J., Henry D.J. and Dutrow B.L. (2011a) Tourmaline as a petrologic forensic mineral: A unique recorder of its geologic past. *Elements*, **7**, 327–332.

van Hinsberg V.J., Henry D.J. and Marschall H.R. (2011b) Tourmaline: an ideal indicator of its host environment. *The Canadian Mineralogist*, **49**, 1–16.

https://doi.org/10.1180/mgm.2022.125 Published online by Cambridge University Press